

Carl Brozek  
Summer, 2008

While early-metal oxo complexes ( $M=O$ ) are common and demonstrate interesting reactivity, late metal complexes are unobserved. Recently, the Hillhouse group synthesized the  $d^8$  imido complex  $1,2\text{-bis}(\text{di-tert-butylphosphino})\text{ethaneNi=NAr}$ . Attempts to synthesize the analogous  $d^8$  oxo led to rapid decomposition to an oxidized phosphine. Though unsuccessful, these results strongly suggested a Ni(II) oxo intermediate. This project will focus on the isolation of a  $Ni=O$  complex by introducing a more rigid backbone in the chelated phosphino ligand to prevent intramolecular migration of phosphorus to oxygen. The reactivity of the  $d^8$  imido complex suggests that the Ni(II) oxo will have interesting reactivity worth investigating.

## In Situ Formation of an Oxygen-Evolving Catalyst in Neutral Water Containing Phosphate and $\text{Co}^{2+}$

Matthew W. Kanan and Daniel G. Nocera\*

Department of Chemistry, 6-335, Massachusetts Institute of Technology, Cambridge, MA 02139-4307, USA.

\*To whom correspondence should be addressed. E-mail: nocera@mit.edu

**The utilization of solar energy on a large scale requires its storage. In natural photosynthesis, energy from sunlight is used to rearrange the bonds of water to  $\text{O}_2$  and  $\text{H}_2$ -equivalents. The realization of artificial systems that perform similar “water splitting” requires catalysts that produce  $\text{O}_2$  from water without the need for excessive driving potentials. Here we report such a catalyst that forms upon the oxidative polarization of an inert indium tin oxide electrode in phosphate-buffered water containing  $\text{Co}^{2+}$ . A variety of analytical techniques indicates the presence of phosphate in an approximate 1:2 ratio with cobalt in this material. The pH dependence of the catalytic activity also implicates  $\text{HPO}_4^{2-}$  as the proton acceptor in the  $\text{O}_2$ -producing reaction. This catalyst not only forms in situ from earth-abundant materials but also operates in neutral water under ambient conditions.**

Sunlight is the only renewable and carbon-neutral energy source of sufficient scale to replace fossil fuels and meet rising global energy demand (1). The diurnal variation in local insolation, however, demands a cost-effective storage of solar energy for its large scale utilization. Of the possible storage methods, nature provides the blueprint for storing sunlight in the form of chemical fuels (1, 2). The primary steps of natural photosynthesis involve the absorption of sunlight and its conversion into spatially separated electron-hole pairs. The holes of this wireless current are then captured by the oxygen evolving complex (OEC) to oxidize water to oxygen and the electrons are captured by photosystem I to reduce  $\text{NADP}^+$  to  $\text{NADPH}$ , nature's form of hydrogen (3). Thus, the overall primary events of photosynthesis store solar energy in a fuel by rearranging the chemical bonds of water to form  $\text{H}_2$  (i.e.,  $\text{NADPH}$ ) and  $\text{O}_2$ .

An approach to duplicating photosynthesis outside of a chloroplast is to convert sunlight into spatially separated electron-hole pairs within a photovoltaic cell and then capture the charges with catalysts that mediate “water splitting” (1, 4). The four holes are captured by a catalyst at the anode to produce oxygen and the four electrons are captured by a

separate catalyst at the cathode to produce hydrogen. The net result is the storage of solar energy in the chemical bonds of  $\text{H}_2$  and  $\text{O}_2$ .

A key determinant of energy storage in artificial photosynthesis is the efficiency of the water-splitting catalysts. Electrocatalysts that are efficient for solar-to-fuels conversion must operate close to the Nernstian potentials (E) for the  $\text{H}_2\text{O}/\text{O}_2$  and  $\text{H}_2\text{O}/\text{H}_2$  half-cell reactions shown in Scheme 1 (half-cell potentials given in the convention of reduction potentials).

The voltage in addition to E that is required to attain a given catalytic activity, referred to as overpotential, limits the efficiency of converting light into catalytic current. Of the two reactions, the  $\text{H}_2\text{O}/\text{O}_2$  reaction is considerably more complex (5). This reaction requires a four-electron oxidation of two water molecules coupled to the removal of four protons to form a relatively weak oxygen-oxygen bond. In addition to controlling this proton-coupled electron transfer (PCET) (6, 7), a catalyst must tolerate prolonged exposure to oxidizing conditions. Even at the thermodynamic limit, water oxidation requires an oxidizing power that causes most chemical functional groups to degrade. Accordingly, the generation of oxygen from water presents a significant challenge toward realizing artificial photosynthesis (8).

The fine-tuned molecular machinery of the OEC oxidizes water at a low overpotential using a  $\text{Mn}_4\text{O}_4\text{Ca}$  cluster (9-12). Outside the OEC, examples of water oxidation catalysts include first-row spinel and perovskite metal oxides, which require concentrated basic solutions ( $\text{pH} > 13$ ) and moderate overpotentials (<400 mV), and precious metals and precious metal oxides, which operate with similar efficiencies under acidic conditions ( $\text{pH} < 1$ ) (13-15). However, few catalysts operate under the conditions of photosynthesis, i.e. in neutral water under ambient conditions. Neutral water is oxidized at Pt electrodes and some precious metal oxides have been reported to operate electrocatalytically in neutral or weakly acidic solutions (16). The development of an earth-abundant, first-row catalyst that operates at pH 7 at low overpotential

remains a fundamental chemical challenge. Here we report an oxygen-evolving catalyst that forms in situ upon anodic polarization of an inert electrode in neutral aqueous phosphate solutions containing  $\text{Co}^{2+}$ . Oxygen generation occurs under benign conditions: pH = 7, 1 atm and room temperature.

Cobalt ions in the presence of chemical oxidants such as  $\text{Ru}(\text{bpy})_3^{3+}$  (bpy = bipyridine;  $E^\circ = 1.25$ ) catalyze the oxidation of water to  $\text{O}_2$  in neutral phosphate solutions (17, 18). Oxygen yields drop in these reactions when oxidized Co species precipitate from solution because the catalytically-active species is removed from the solution-phase reaction. However, an oxidation-induced precipitation may be exploited to prepare electrocatalysts in situ if the precipitated material remains catalytically active and can be oxidized at an electrode surface. To explore this possibility for Co-catalyzed water oxidation, we examined electrochemical oxidations of aqueous solutions containing phosphate and  $\text{Co}^{2+}$ . Cyclic voltammetry of a 0.5 mM solution of  $\text{Co}(\text{NO}_3)_2$  in 0.1 M potassium phosphate pH 7.0 (KPi electrolyte) exhibits an oxidation wave at  $E_p = 1.13$  V vs. the normal hydrogen electrode (NHE) followed by the onset of a strong catalytic wave at 1.23 V. (Fig. 1A). A broad, relatively weak reduction wave is observed on the cathodic scan. The presence of a catalytic wave prompted us to examine the electrode activity during controlled-potential electrolysis.

Indium-tin-oxide (ITO) was used as the electrode for bulk electrolysis to ensure a minimal background activity for  $\text{O}_2$  production. An electrolysis at 1.29 V without stirring in neutral KPi electrolyte containing 0.5 mM  $\text{Co}^{2+}$  exhibits a rising current density that reaches a peak value  $>1$  mA/cm<sup>2</sup> after 7 to 8 h (Fig. 1B). During this time, a dark coating forms on the ITO surface and effervescence from this coating becomes increasingly vigorous (19). The same results are observed with either  $\text{CoSO}_4$ ,  $\text{Co}(\text{NO}_3)_2$ , or  $\text{Co}(\text{OTf})_2$  as the  $\text{Co}^{2+}$  source, which indicates that the original  $\text{Co}^{2+}$  counterion is unimportant and that this activity does not depend on an impurity found in a specific source. The amount of charge passed during the course of an 8 h electrolysis far exceeds what could be accounted for by stoichiometric oxidation of the  $\text{Co}^{2+}$  in solution (20). These observations are indicative of the in situ formation of an oxygen evolving catalyst. Catalyst formation also proceeds on a fluorine-tin-oxide (FTO) electrode and if KPi is replaced by NaPi electrolyte. In a control experiment, the current density during bulk electrolysis under identical conditions in the absence of  $\text{Co}^{2+}$  rapidly drops to a baseline level of  $\sim 25$  nA/cm<sup>2</sup> (Fig. 1B, inset).

The morphology of the electrode coating formed during electrolysis in the presence of  $\text{Co}^{2+}$  was examined by scanning electron microscopy (SEM). The electrodeposited material consists of particles that have coalesced into a thin

film and individual micrometer-sized particles on top of the film (Fig. 2A). The ITO substrate can be seen through cracks in the film that form upon drying, as evidenced by particles that are split into complementary pieces. The film thickness gradually increases over the course of the electrodeposition (see fig. S4 for additional images). At maximum activity under these electrolysis conditions, the film is  $>2$   $\mu\text{m}$  thick. The x-ray powder diffraction pattern of an electrodeposited catalyst shows broad amorphous features and no peaks indicative of crystalline phases other than the peaks associated with the ITO layer (fig. S1).

In the absence of detectable crystallites, the composition of the electrodeposited material was analyzed by three complementary techniques. Energy-dispersive x-ray analysis (EDX) spectra were obtained from multiple 100 to 300  $\mu\text{m}^2$  regions of several independently prepared samples. These spectra identify Co, P, K and O as the principal elemental components of the material (Fig. 2B). Although the material's morphology is not ideally suited for quantitative EDX, the analyses consistently indicate a Co:P:K ratio between  $\sim 2:1:1$  and  $3:1:1$ . To obtain an independent determination of elemental composition, electrolysis was performed with several larger ITO electrodes; the deposited material was scraped off and combined for a total yield of  $\sim 3$  mg. Microanalytical elemental analysis of the combined material indicates 31.1% Co, 7.70% P and 7.71% K, corresponding to a 2.1:1.0:0.8 Co:P:K ratio. Finally, the surface of an electrodeposited catalyst on the ITO substrate was analyzed by x-ray photoelectron spectroscopy (XPS). All peaks in the XPS spectra are accounted for by the elements detected above in addition to In and Sn from the ITO substrate. The high-resolution P 2p peak at 133.1 eV is consistent with phosphate. The Co 2p peaks at 780.7 eV and 795.7 eV are in a range typical of  $\text{Co}^{2+}$  or  $\text{Co}^{3+}$  bound to oxygen (fig. S2) (21). Together, the XRD and analytical results indicate that electrolysis of a  $\text{Co}^{2+}$  solution in neutral KPi electrolyte results in the electrodeposition of an amorphous Co oxide or hydroxide incorporating a substantial amount of phosphate anion at a stoichiometric ratio of roughly 2:1:1 for Co:P:K.

Three experiments were performed to establish that the catalytic activity observed with this material corresponds to authentic water oxidation. Each of these experiments was performed in neutral KPi electrolyte in the absence of  $\text{Co}^{2+}$ . Catalyst coatings ( $\sim 1.3$  cm<sup>2</sup>) were prepared in a preliminary step as described above and stored under ambient laboratory conditions until used.

To confirm that water is the source of the  $\text{O}_2$  produced, electrolysis was performed in helium-saturated electrolyte containing 14.6%  $^{18}\text{OH}_2$  in a gas-tight electrochemical cell in line with a mass spectrometer. The helium carrier gas was continuously flowed through the headspace of the anodic compartment into the mass spectrometer and the relative

abundances of  $^{32}\text{O}_2$ ,  $^{34}\text{O}_2$ , and  $^{36}\text{O}_2$  were monitored at 2 s intervals. Within minutes of initiating electrolysis at 1.29 V, the signals for the three isotopes began to rise above their background levels as the  $\text{O}_2$  produced by the catalyst escaped into the headspace. Upon terminating the electrolysis 1 hour later, these signals slowly returned to their background levels (Fig. 3A). The  $^{32}\text{O}_2$ ,  $^{34}\text{O}_2$ , and  $^{36}\text{O}_2$  isotopes were detected in the statistical ratio (72.9%, 24.9%, and 2.1% relative abundances, respectively, Fig. 3B).

The Faradaic efficiency of the catalyst was measured by using a fluorescence-based  $\text{O}_2$  sensor. Electrolysis was performed in KPi electrolyte in a gas-tight electrochemical cell under an  $\text{N}_2$  atmosphere with the sensor placed in the headspace. After initiating electrolysis at 1.29 V, the percentage of  $\text{O}_2$  detected in the headspace rose in accord with what was predicted by assuming that all of the current was caused by  $4e^-$  oxidation of water to produce  $\text{O}_2$  (Fig. 3C). The amount of  $\text{O}_2$  produced (95  $\mu\text{moles}$ , 3.0 mg) greatly exceeds the amount of catalyst (~0.2 mg), which shows no perceptible decomposition during the course of the experiment.

The stability of phosphate under catalytic conditions was assayed by  $^{31}\text{P}$  NMR. Electrolysis in a two compartment cell with 10 mL of KPi electrolyte (1 mmol of phosphate) on each side was allowed to proceed until 45 C had been passed through the cell (0.46 mmol electrons). Electrolysis solutions from both chambers show single, clean  $^{31}\text{P}$  resonances, which indicate that the electrolyte is robust under these conditions (fig. S3). Together, the mass spectrometry, Faradaic efficiency, and  $^{31}\text{P}$  NMR results demonstrate that the electrodeposited catalyst cleanly oxidizes  $\text{H}_2\text{O}$  to  $\text{O}_2$  in neutral KPi solutions.

The current density of a catalyst on ITO was measured as a function of the overpotential ( $\eta$ ) in KPi electrolyte without  $\text{Co}^{2+}$  (Fig. 4A, black dots). At pH 7.0, appreciable catalytic current is observed beginning at  $\eta = 0.28$  V and a current density of 1  $\text{mA}/\text{cm}^2$  (corresponding to 9  $\mu\text{mol O}_2 \text{cm}^{-2} \text{h}^{-1}$ ) requires  $\eta = 0.41$  V. The Tafel plot deviates slightly from linearity, possibly reflecting an uncompensated iR drop caused by the surface resistivity of the ITO (8 to 12  $\text{ohm}/\text{sq}$ ). Substantial improvements in the activity profile may be attainable without changing the catalyst composition by depositing on alternative substrates or improving ohmic contact to the ITO.

The catalyst used to obtain the Tafel plot at pH 7 was subsequently transferred to KPi electrolyte at pH 4.6 and the current density was measured at a constant applied potential (1.24 V) while the pH was increased incrementally to 9.4 by adding aliquots of concentrated KOH. A plot of the log of current density vs. pH exhibits a steep initial rise that levels off in the high pH range such that increasing the pH from 8 to 9.4 at this applied potential has little effect (Fig. 4B). These

data can be converted to a Tafel plot by using Eq. 1 (Scheme 1) and accounting for iR drop (Fig. 4 caption). A comparison to the Tafel plot obtained at pH 7 indicates that the catalyst exhibits approximately Nernstian behavior from pH 5 to 8: Increasing the pH by one unit at constant applied potential (1.24 V) has approximately the same effect as increasing the overpotential by 0.059 V at pH 7 (Fig. 4A, red dots). This result implicates a reversible  $ne^-, nH^+$  removal prior to the rate-determining step for  $\text{O}_2$  evolution in this pH range. Thus, an important component of the activity at pH 7 with this catalyst is the existence of one or more intermediates preceding  $\text{O}_2$  formation that are deprotonated reversibly by  $\text{HPO}_4^{2-}$  in a PCET event (22). The pH-independent behavior above pH 8 at the applied potential indicates a change in mechanism, most likely involving a deprotonated intermediate.

In addition to mediating the deprotonation required for catalysis, the KPi electrolyte provides a medium for in situ catalyst formation. Given that phosphate is a structural element, and that the catalyst forms under oxidizing conditions, it is plausible that deposition is driven by the interaction of phosphate and  $\text{Co}^{3+}$ . By judicious choice of other metal-anion pairs or combinations of multiple metals and anions, it may be possible to access other oxygen-evolving catalysts that form in situ and operate in neutral solutions. In situ formation is advantageous because, in principle, it enables catalyst deposition on a variety of substrates, including those that are too delicate to tolerate traditional catalyst preparation techniques. This attribute is important for interfacing a catalyst with a variety of electrochemical or photoelectrochemical cell designs.

In situ formation also implies a self-repair mechanism. Molecular mechanisms involving  $\text{O}_2/\text{H}_2\text{O}$  cycles at Co centers would suggest that catalytic reactions cycle among  $\text{Co}^{2+}$ ,  $\text{Co}^{3+}$  and  $\text{Co}^{4+}$ -oxo oxidation states (17, 23). The propensity of metal ion dissolution has been shown to correlate with ligand substitution (24). Given that  $\text{Co}^{3+}$  is substitutionally inert relative to  $\text{Co}^{2+}$ , a dynamic equilibrium between  $\text{Co}^{2+}\text{-HPO}_4^{2-}$  in solution and  $\text{Co}^{3+}\text{-HPO}_4^{2-}$  on the anodically poised electrode may be established. More generally, if a catalytic cycle involves an oxidation state that is prone to dissolution, this process can be countered by continual catalyst formation by establishing an equilibrium with the judicious choice of an anion.

The results reported herein highlight a new area of exploration for the development of easily-prepared, earth-abundant catalysts that oxidize water. If artificial photosynthesis is to enable the storage of solar energy commensurate with global demand, water-splitting chemistry will need to be performed at a daunting scale. Storing the equivalent of the current energy demand would require splitting greater than  $10^{15}$  mol/yr of water, which is roughly

100 times the scale of nitrogen fixation by the Haber Bosch process. The conditions under which water splitting is performed will determine how solar energy is deployed. The catalyst reported here has many elements of natural photosynthesis including its formation from earth abundant metal ions in aqueous solution, a plausible pathway for self-repair, a carrier for protons in neutral water and the generation of O<sub>2</sub> at low overpotential, neutral pH, 1 atm and room temperature.

## References and Notes

1. N. S. Lewis, D. G. Nocera, *Proc. Natl. Acad. Sci. U.S.A.* **103**, 15729 (2006).
2. N. Nelson, A. Ben-Shem, *Nat. Rev. Mol. Cell Biol.* **5**, 971 (2004).
3. J. Barber, *Phil. Trans. Roy. Soc. A* **365**, 1007 (2007).
4. A. J. Bard, M. A. Fox, *Acc. Chem. Res.* **28**, 141 (1995).
5. T. A. Betley, Q. Wu, T. Van Voorhis, D. G. Nocera, *Inorg. Chem.* **47**, 1849 (2008).
6. R. I. Cukier, D. G. Nocera, *Annu. Rev. Phys. Chem.* **49**, 337 (1998).
7. M. H. V. Huynh, T. J. Meyer, *Chem. Rev.* **107**, 5004 (2007).
8. R. Eisenberg, H. B. Gray, *Inorg. Chem.* **47**, 1697 (2008).
9. K. N. Ferreira, T. M. Iverson, K. Maghlaoui, J. Barber, S. Iwata, *Science* **303**, 1831 (2004).
10. S. Iwata, J. Barber, *Curr. Opin. Struct. Biol.* **14**, 447 (2004).
11. J. Yano *et al.*, *Science* **314**, 821 (2006).
12. B. Loll, J. Kern, W. Saenger, A. Zouni, J. Biesiadka, *Nature* **438**, 1040 (2005).
13. S. Trasatti, in *Electrochemistry of Novel Materials*, J. Lipkowsky, P. N. Ross, Eds. (VCH, New York, Ch. 5, 1994).
14. J. O. Bockris, T. J. Otagawa, *J. Electrochem. Soc.* **131**, 290 (1984).
15. M. R. Tarasevich, B. N. Efremov, in *Electrodes of Conductive Metal Oxides*, S. Trasatti, Ed. (Elsevier, Amsterdam, Ch. 5, 1980).
16. M. Yagi, E. Tomita, S. Sakita, T. Kuwabara, K. Nagai, *J. Phys. Chem. B.* **109**, 21489 (2005).
17. V. Y. Shafirovich, N. K. Khannanov, V. V. Strelets, *Nouv. J. Chim.* **4**, 81 (1980).
18. B. S. Brunshwig, M. H. Chou, C. Creutz, P. Ghosh, N. Sutin, *J. Am. Chem. Soc.* **105**, 4832 (1983).
19. Materials and methods, videos of an active electrode, and figs. S1 to S4 are available as supporting material on Science Online.
20. In a typical experiment, >40 C are passed over 8 h, whereas oxidation of all the Co<sup>2+</sup> in solution requires 1.9 C per oxidation state change.
21. K. D. Bomben, J. F. Moulder, P. E. Sobol, W. F. Stickel, in *Handbook of X-Ray Photoelectron Spectra: A Reference*

*Book of Standard Spectra for Identification*, J. Chastain, Ed. (Perkin Elmer, Eden Prairie, MN, 1992).

22. T. Irebo, S. Y. Reece, M. Sjödin, D. G. Nocera, L. Hammarström, *J. Am. Chem. Soc.* **129**, 154622 (2007).
23. C. J. Chang, Z.-H. Loh, C. Shi, F. C. Anson, D. G. Nocera, *J. Am. Chem. Soc.* **126**, 10013 (2004).
24. W. H. Casey, *J. Coll. Inter. Sci.* **146**, 586 (1991).
25. Supported by a grant from the National Science Foundation, Chemical Bonding Center (CHE-0802907). M.W.K. is supported by a Ruth L. Kirchenstein NRSA Postdoctoral Fellowship provided by the NIH (F32GM07782903). We thank E. Shaw for obtaining XPS spectra, G. Henoch for providing the videos in the SOM, and Y. Surendranath for many productive discussions.

## Supporting Online Material

[www.sciencemag.org/cgi/content/full/1162018/DC1](http://www.sciencemag.org/cgi/content/full/1162018/DC1)

Materials and Methods

Figs. S1 to S4

Movies S1 and S2

19 June 2008; accepted 18 July 2008

Published online 31 July 2008; 10.1126/science.1162018

Include this information when citing this paper.

**Fig. 1.** (A) Cyclic voltammogram in 0.1 M KPi electrolyte at pH 7.0 with no Co<sup>2+</sup> ion present (black line), and with 0.5 mM Co<sup>2+</sup> present (red line). The potential was measured against a Ag/AgCl reference and converted to normal hydrogen electrode (NHE) potentials by using E(NHE) = E(Ag/AgCl) + 0.192 V. (B) Current density profile for bulk electrolysis at 1.29 V (vs. NHE) in 0.1 M KPi electrolyte at pH 7.0 containing 0.5 mM Co<sup>2+</sup>. (Inset) Profile in the absence of Co<sup>2+</sup>.

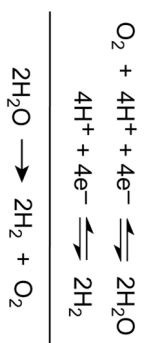
**Fig. 2.** (A) SEM image (30° tilt) of the electrodeposited catalyst after 30 C/cm<sup>2</sup> were passed in 0.1 M KPi electrolyte at pH 7.0, containing 0.5 mM Co<sup>2+</sup>. The ITO substrate can be seen through cracks in the dried film. (B) Typical EDX spectrum acquired at 12 kV.

**Fig. 3.** (A) Mass spectrometric detection of isotopically-labeled <sup>16,16</sup>O<sub>2</sub> (black line), <sup>16,18</sup>O<sub>2</sub> (blue line) and <sup>18,18</sup>O<sub>2</sub> (red line) during electrolysis of a catalyst film on ITO in KPi electrolyte containing 14.6% <sup>18</sup>OH<sub>2</sub>. Green arrow indicates initiation of electrolysis at 1.29 V (NHE) and red arrow indicates termination of electrolysis. Inset: expansion of the <sup>18,18</sup>O<sub>2</sub> signal. (B) Percent abundance of each isotope over the course of the experiment. Average observed abundance ±2σ indicated above each line. Statistical abundances: 72.9%, 24.9%, and 2.1%. (C) O<sub>2</sub> production measured by fluorescent sensor (red line) and the theoretical amount of O<sub>2</sub> produced (blue line) assuming a Faradic efficiency of 100%. Green

arrow indicates initiation of electrolysis at 1.29 V and red arrow indicates termination of electrolysis

**Fig. 4.** (A) Tafel plot (black dots),  $\eta = (V_{\text{appl}} - iR) - E(\text{pH } 7)$ , of a catalyst film on ITO in 0.1 M KPi electrolyte pH 7.0, corrected for the  $iR$  drop of the solution. pH data converted into a Tafel plot (red dots),  $\eta = (V_{\text{appl}} + 0.059\Delta\text{pH} - iR) - E(\text{pH } 7)$ , assuming Nernstian behavior and correcting for  $iR$  drop of the solution. The pH = 5 and pH = 8 data points are indicated by arrows. (B) Current density dependence on pH in 0.1 M KPi electrolyte. The green line shows the calculated mole fraction of  $\text{HPO}_4^{2-}$ . The potential was set at 1.24 V (vs. NHE) with no  $iR$  compensation.

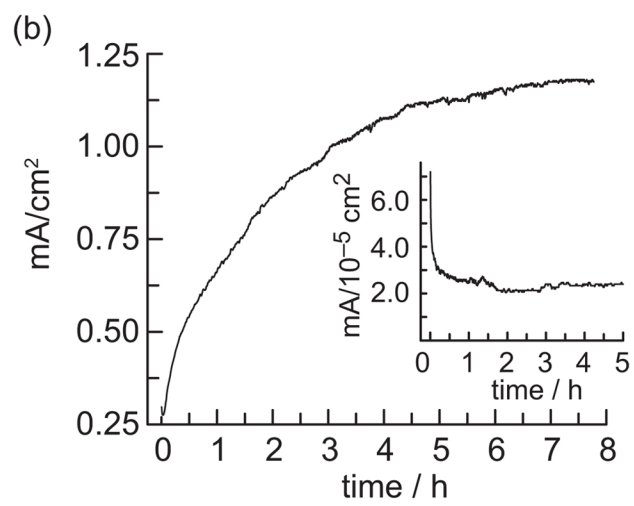
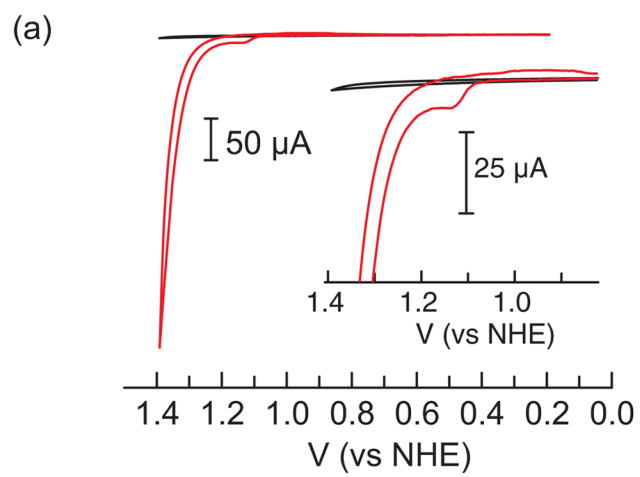
Scheme 1

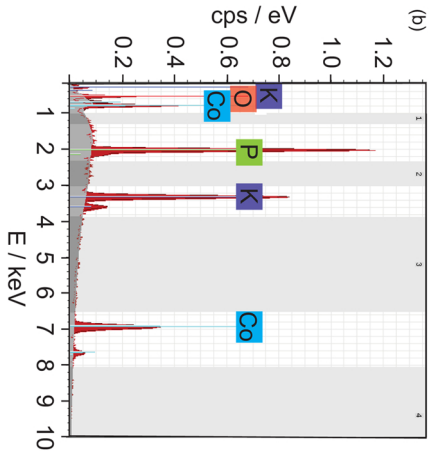
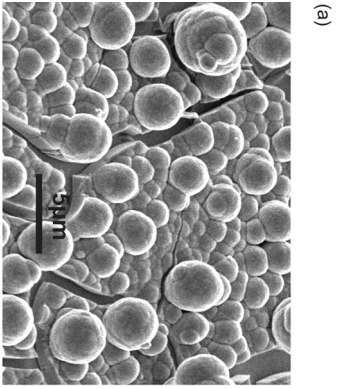


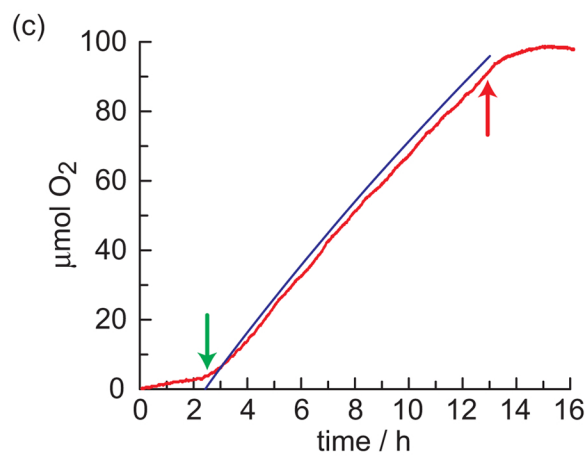
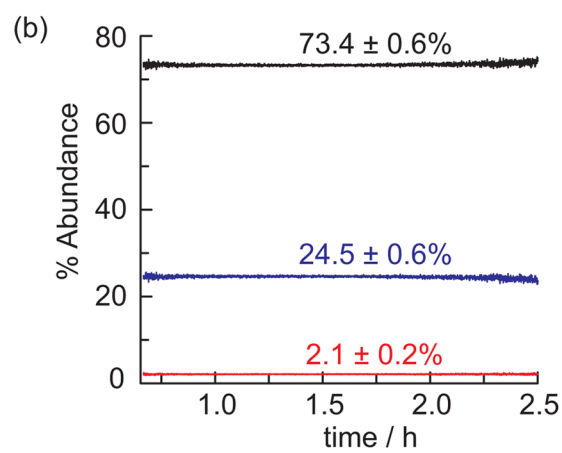
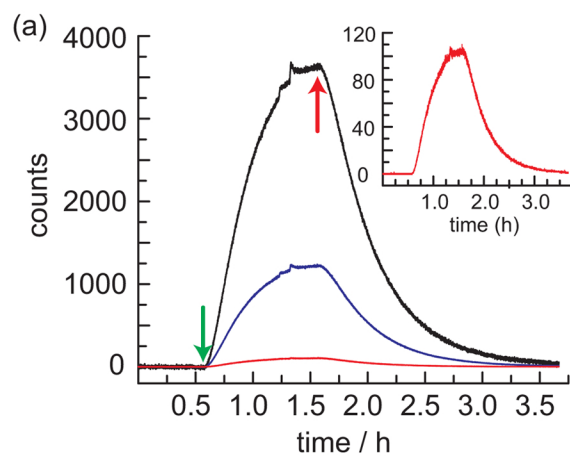
$$E_{\text{anode}} = 1.23 \text{ V} - 0.059 (\text{pH}) \text{ V vs NHE}$$

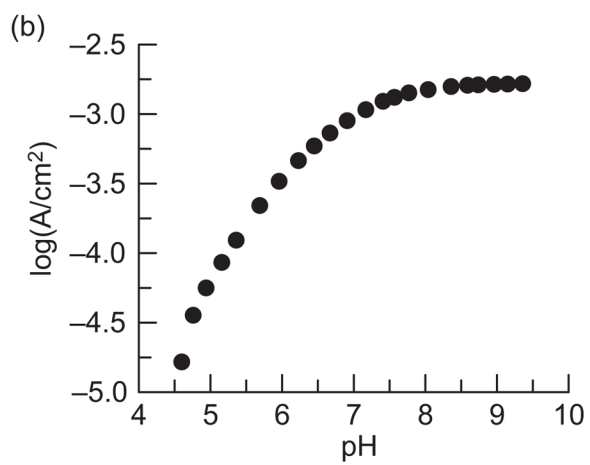
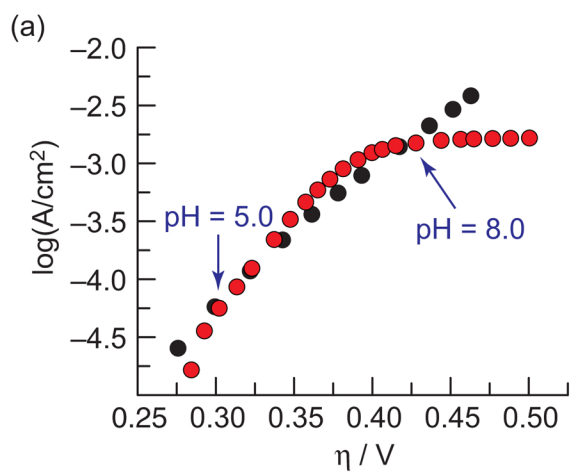
$$E_{\text{cathode}} = 0 \text{ V} - 0.059 (\text{pH}) \text{ V vs NHE}$$

$$E_{\text{rxn}} = -1.23 \text{ V}$$









## Terminal Amido and Imido Complexes of Three-Coordinate Nickel

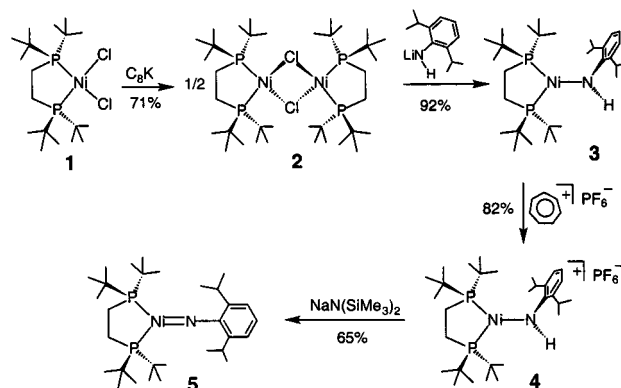
Daniel J. Mindiola and Gregory L. Hillhouse\*

Searle Chemistry Laboratory, Department of Chemistry  
The University of Chicago, Chicago, Illinois 60637

Received February 9, 2001

The chemistry of late-transition-metal complexes possessing amido ( $\text{NR}_2^-$ ) and imido ( $\text{NR}^{2-}$ ) ligands is much less developed than that of the early- and mid-transition elements.<sup>1</sup> This is particularly true of the nickel triad, where the contrast between these hard, nitrogen-donor ligands and the soft, electron-rich metals is considered to be energetically destabilizing and is exacerbated by the general lack of stabilizing  $\pi$ -donor interactions involving the ligand lone pair(s) that are commonly found with terminal amides and imides of the early- and mid-transition metals. There has been increasing research activity in this area by us and others,<sup>2–4</sup> and it has been demonstrated that amido complexes of Ni and Pd play key roles in a range of important reactions.<sup>5</sup> Imido complexes of the Ni triad are limited to a few bimetallic and trimetallic examples possessing bridging ( $\mu_2$  and  $\mu_3$ )  $\text{NR}^{2-}$  moieties.<sup>6,7</sup> Stone's 1970 report of  $(\text{Ph}_2\text{MeP})_2\text{M}=\text{NCF}_2\text{CFHCF}_3$  ( $\text{M} = \text{Pd}, \text{Pt}$ ) complexes incorporating an imido ligand with a strongly electron-withdrawing fluoropropyl substituent provides the only examples of terminal Group 10 imido derivatives, although characterization was limited to  $^1\text{H}$  and  $^{19}\text{F}$  NMR spectroscopic data, and the exact nature of these compounds is unclear.<sup>8</sup> To date, the only structurally characterized examples of late-metal complexes possessing terminal imido ligands are Bergman's Ir derivatives of the general formulation  $\text{Cp}^*\text{Ir}\equiv\text{NR}$  ( $\text{R} = \text{aryl}, \text{alkyl}, \text{silyl}$ ).<sup>9</sup>

### Scheme 1



In the course of our studies of the reactions of aryl azides with Ni(II) alkyls to give amide moieties,<sup>2</sup> we have noted that azides with bulky substituents (i.e., mesityl azide) yield products that suggest involvement of nitrene (or imido) intermediates.<sup>10</sup> Moreover, a recent report from Jones and Vivic presented compelling evidence that a reactive terminal sulfido complex of Ni(II) was generated on thermolysis of  $(\text{PR}_2\text{CH}_2\text{CH}_2\text{PR}_2)\text{Ni}(\text{SH})(\text{Ph})$ , although it was unstable with respect to dimerization via Ni–S–Ni bridges.<sup>11</sup> Herein we report a successful synthetic strategy for the preparation of monomeric, three-coordinate nickel complexes containing the chelating 1,2-bis(di-*tert*-butylphosphino)ethane (dtbpe) ligand and an amido or imido nitrogen-donor ligand, along with the structural characterization of the first terminal imido complex of nickel, a species which features a nickel–nitrogen multiple bond.

Our initial approach to preparing a terminal imido complex of Ni(II) involved a modification of Jones' method for the synthesis of the transient " $\text{L}_2\text{Ni}=\text{S}$ " (described above).<sup>11</sup> Specifically, we wished to effect deprotonation or dehydrohalogenation of an appropriate Ni(II) amide (i.e.,  $\text{L}_x\text{Ni}(\text{NHR})\text{X}$ ). To inhibit imido bridging, we used bulky substituents in both the ancillary phosphine ligand (dtbpe) as well as at nitrogen. Reaction of (dtbpe)NiCl<sub>2</sub> (**1**)<sup>12</sup> with 1 equiv of lithium 2,6-di-*iso*-propylphenylamide ( $\text{LiNH}(2,6-(\text{CHMe})_2\text{C}_6\text{H}_3)$ ) gives a mixture of products, including paramagnetic species. Reduction of **1** with  $\text{KC}_8$  in THF at  $-35^\circ\text{C}$  gives red crystals of the Ni(I) monochloride  $[(\text{dtbpe})\text{NiCl}]_2$  (**2**) in 71% yield.<sup>13</sup> Related Ni(I) chlorides of chelating diphosphine ligands have been reported.<sup>14</sup> In contrast to **1**, toluene solutions of **2** react cleanly at  $-35^\circ\text{C}$  with  $\text{Et}_2\text{O}$  solutions of lithium 2,6-di-*iso*-propylphenylamide to afford the paramagnetic arylamido complex  $(\text{dtbpe})\text{Ni}\{\text{NH}(2,6-(\text{CHMe})_2\text{C}_6\text{H}_3)\}$  (**3**) as beet-red crystals in 92% yield (Scheme 1). This Ni(I) complex has been characterized by elemental analysis, IR and  $^1\text{H}$  NMR spectroscopic methods,<sup>13</sup> and by single-crystal X-ray diffraction.<sup>15</sup> The molecular structure of **3** features a planar, three-coordinate

(10) Lin, B.; Hillhouse, G. L. *Abstracts of Papers, 213th ACS National Meeting*; San Francisco, CA, April, 1997; Abstract INOR 636. (b) Lin, B. L. Ph.D. Thesis, The University of Chicago (Chicago, IL), December, 2000.

(11) (a) Vivic, D. A.; Jones, W. D. *J. Am. Chem. Soc.* **1999**, *121*, 4070. (b) Vivic, D. A.; Jones, W. D. *J. Am. Chem. Soc.* **1999**, *121*, 7606.

(12) Bach, I.; Goddard, R.; Kopsiske, C.; Seevogel, K.; Pörschke, K.-R. *Organometallics* **1999**, *18*, 10.

(13) See the Supporting Information for complete spectroscopic and analytical details for **2–5** and solution magnetic moments for **2** and **3**.

(14) Scott, F.; Krüger, C.; Betz, P. *J. Organomet. Chem.* **1990**, *387*, 113.

(15) Crystal data for **3**:  $\text{C}_{30}\text{H}_{58}\text{N}_2\text{NiP}_2$ , orthorhombic,  $P2_12_12_1$ ,  $a = 10.8603(9)$  Å,  $b = 16.6536(14)$  Å,  $c = 17.3090(14)$  Å,  $Z = 4$ ,  $\mu(\text{Mo K}\alpha) = 7.40 \text{ cm}^{-1}$ ,  $T = 100 \text{ K}$ ,  $V = 3130.6(4) \text{ \AA}^3$ ,  $\lambda = 0.71073 \text{ \AA}$ ,  $D_c = 1.174 \text{ mg/mm}^3$ . Of 19258 data collected (red crystal,  $1.70 \leq \theta \leq 28.29$ ) 7365 were independent and observed with  $I > 2\sigma(I)$ . Flack  $x$  parameter =  $-0.004$ , 0.010 esd. All non-hydrogen atoms were anisotropically refined, and hydrogen atoms were idealized except for the H attached to N, which was located and refined isotropically.  $R(F) = 0.035$  and  $R(wF^2) = 0.063$ .

(1) (a) Wigley, D. E. *Prog. Inorg. Chem.* **1994**, *42*, 239. (b) Fryzuk, M. D.; Montgomery, C. D. *Coord. Chem. Rev.* **1989**, *95*, 1. (c) Bryndza, H. E.; Tam, W. *Chem. Rev.* **1988**, *88*, 1163. (d) Lappert, M. F.; Power, P. P.; Sanger, A. R.; Srivastava, R. C. *Metal and Metalloid Amides*; Ellis Horwood: Chichester, 1980. (e) Power, P. P. *Comments Inorg. Chem.* **1989**, *8*, 177.

(2) (a) Matsunaga, P. T.; Hess, C. R.; Hillhouse, G. L. *J. Am. Chem. Soc.* **1994**, *116*, 3665. (b) Koo, K.; Hillhouse, G. L. *Organometallics* **1995**, *14*, 4421. (c) Koo, K.; Hillhouse, G. L. *Organometallics* **1996**, *15*, 2669.

(3) Examples of Group 10 amides: (a) Bradley, D. C.; Hursthouse, M. B.; Smallwood, R. J.; Welch, A. J. *J. Chem. Soc., Chem. Commun.* **1972**, 872. (b) Fryzuk, M. D.; MacNeil, P. A. *J. Am. Chem. Soc.* **1981**, *103*, 3592. (c) Fryzuk, M. D.; MacNeil, P. A.; Rettig, S. J.; Secco, A. S.; Trotter, J. *Organometallics* **1982**, *1*, 918. (d) Hope, H.; Olmstead, M. M.; Murray, B. D.; Power, P. P. *J. Am. Chem. Soc.* **1985**, *107*, 712. (e) Bartlett, R. A.; Chen, H.; Power, P. P. *Angew. Chem., Int. Ed. Engl.* **1989**, *28*, 316. (f) Villanueva, L. A.; Abboud, K. A.; Boncella, J. M. *Organometallics* **1994**, *13*, 3921. (g) VanderLende, D. D.; Abboud, K. A.; Boncella, J. M. *Inorg. Chem.* **1995**, *34*, 5319. (h) VanderLende, D. D.; Boncella, J. M.; Abboud, K. A. *Acta Crystallogr., Sect. C* **1995**, *51*, 591. (i) Cowan, R. L.; Trogler, W. C. *J. Am. Chem. Soc.* **1989**, *111*, 4750. (j) Seligson, A. L.; Cowan, R. L.; Trogler, W. C. *Inorg. Chem.* **1995**, *34*, 5319. (k) Driver, M. S.; Hartwig, J. F. *J. Am. Chem. Soc.* **1997**, *119*, 8232. (l) Bryndza, H. E.; Fultz, W. C.; Tam, W. *Organometallics* **1985**, *4*, 939. (m) Klein, H.; Karsch, H. H. *Chem. Ber.* **1973**, *106*, 2438.

(4) (a) Holland, P. L.; Andersen, R. A.; Bergman, R. G.; Huang, J.; Nolan, S. P. *J. Am. Chem. Soc.* **1997**, *119*, 12800 and references therein. (b) Holland, P. L.; Smith, M. E.; Andersen, R. A.; Bergman, R. G. *J. Am. Chem. Soc.* **1997**, *119*, 12815. (c) Holland, P. L.; Andersen, R. A.; Bergman, R. G. *J. Am. Chem. Soc.* **1996**, *118*, 1092.

(5) (a) Yang, B. H.; Buchwald, S. L. *J. Organomet. Chem.* **1999**, *576*, 125. (b) Hartwig, J. F. *Pure Appl. Chem.* **1999**, *71*, 1417. (c) Wolfe, J. P.; Wagaw, S.; Marcoux, J. F.; Buchwald, S. L. *Acc. Chem. Res.* **1998**, *31*, 805. (d) Hartwig, J. F. *Acc. Chem. Res.* **1998**, *31*, 852.

(6) Meij, R.; Stufkens, D. J.; Vrieze, K.; Brouwers, A. M. F.; Overbeek, A. R. *J. Organomet. Chem.* **1978**, *155*, 123.

(7) (a) Otsuka, S.; Nakamura, A.; Yoshida, T. *Inorg. Chem.* **1968**, *7*, 261. (b) Muller, J.; Dörner, H.; Köhler, F. H. *Chem. Ber.* **1973**, *106*, 1122. (c) Klein, H.-F.; Haller, S.; König, H.; Dartiguenave, Y.; Menu, M.-J. *J. Am. Chem. Soc.* **1991**, *113*, 4673.

(8) McGlinchey, M. J.; Stone, F. G. A. *J. Chem. Soc., Chem. Commun.* **1970**, 1265.

(9) (a) Gleuck, D. S.; Wu, J.; Hollander, F. J.; Bergman, R. G. *J. Am. Chem. Soc.* **1991**, *113*, 2041. (b) Gleuck, D. S.; Hollander, F. J.; Bergman, R. G. *J. Am. Chem. Soc.* **1989**, *111*, 2719.

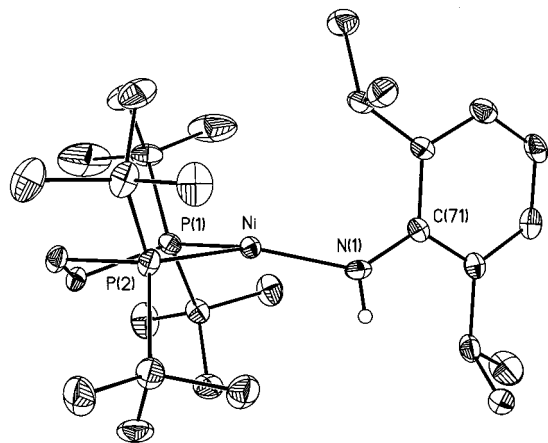


**Figure 1.** A perspective view of the molecular structure of **3** showing the atom-labeling scheme. H-atoms (except H(1)) have been omitted for clarity. Selected metrical parameters: Ni–P(1) = 2.2094(8), Ni–P(2) = 2.2012(7), Ni–N(1) = 1.881(2), N(1)–C(71) = 1.373(3), N(1)–H(1) = 0.82(2) Å; P(1)–Ni–P(2) = 91.91(3), P(1)–Ni–N(1) = 123.18(7), P(2)–Ni–N(1) = 140.41(7), Ni–N(1)–C(71) = 134.6(2), Ni–N(1)–H(1) = 111(2), C(71)–N(1)–H(1) = 109(2)°.

nickel and a terminal, planar amido ligand (Ni–N(1) = 1.881(2) Å) (see Figure 1). The {P(1), P(2), Ni} and {N(1), C(71), H(1)} planes are orthogonal with a 91° dihedral angle. The Ni–N distance is comparable to those found for other terminal Ni amides, such as the related three-coordinate Ni(I) complex (PPh<sub>3</sub>)<sub>2</sub>–Ni{N(SiMe<sub>2</sub>)<sub>2</sub>} (Ni–N = 1.88(1) Å)<sup>3a</sup> and several diverse Ni(II) examples having (Ni–N)<sub>avg</sub> ≈ 1.88 Å (ranging from 1.93 to 1.82 Å).<sup>3c–e,h,4b</sup>

Recognizing that moving from the Ni(I) to Ni(II) manifold should prove advantageous in preparing a terminal imido moiety since a three-coordinate, d<sup>8</sup> species could be stabilized by ligand-to-metal  $\pi$ -donation, we sought to chemically oxidize **3** by one electron. Common oxidants such as Cp<sub>2</sub>Fe<sup>+</sup>, Ag<sup>+</sup>, or I<sub>2</sub> gave myriad decomposition products, consistent with observations that these oxidants are competent in triggering oxidatively induced reductive elimination from alkyl Ni(II) amides and alkoxides via Ni(III) intermediates.<sup>2,16</sup> A cyclic voltammogram of a solution of **3** (THF/TBAH) shows two closely spaced, quasireversible oxidations at  $E_{1/2} = -0.90$  V and  $-0.52$  V (relative to Fc/Fc<sup>+</sup>) for the Ni(I)/Ni(II) and Ni(II)/Ni(III) couples, respectively. These electrochemical data suggest that to effect the oxidation of **3** to Ni(II), a very weak oxidant whose potential lies in this narrow range is required to avoid over-oxidation to Ni(III). Inspection of tabulations of oxidation potentials of reagents indicated a good choice might be tropylium, having  $E^0 = -0.65$  V in acetonitrile.<sup>17</sup> Accordingly, oxidation of THF solutions of **3** with tropylium hexafluorophosphate at  $-35$  °C gives the diamagnetic Ni(II) amido salt [(dtbpe)Ni{NH(2,6-(CHMe<sub>2</sub>)<sub>2</sub>C<sub>6</sub>H<sub>3</sub>)<sup>+</sup>}[PF<sub>6</sub><sup>−</sup>] (**4**) as dark-green crystals in 82% isolated yield (Scheme 1). **4** was characterized by elemental analysis, IR and NMR (<sup>1</sup>H, <sup>13</sup>C, <sup>19</sup>F, <sup>31</sup>P) spectroscopy,<sup>13</sup> and single-crystal X-ray diffraction. Although disordered, the structure of **4** shows well-separated cations and anions; the coordination geometry about Ni is similar to that observed in **3**, with a Ni–N bond length of 1.768(14) Å.<sup>18</sup>

(16) (a) Matsunaga, P. T.; Hillhouse, G. L.; Rheingold, A. L. *J. Am. Chem. Soc.* **1993**, *115*, 2075. (b) Matsunaga, P. T.; Mavropoulos, J. C.; Hillhouse, G. L. *Polyhedron* **1995**, *14*, 175. (c) Koo, K.; Hillhouse, G. L.; Rheingold, A. L. *Organometallics* **1995**, *14*, 456. (d) Han, R.; Hillhouse, G. L. *J. Am. Chem. Soc.* **1997**, *119*, 8135. (e) Koo, K.; Hillhouse, G. L. *Organometallics* **1998**, *17*, 2924.

(17) Connelly, N. G.; Geiger, W. E. *Chem. Rev.* **1996**, *96*, 877.

(18) The structure of **4** suffered from conformational disorder of the *tert*-Bu and CH<sub>2</sub> groups of the dtbpe ligand, and the *iso*-Pr groups of the amido ligand. A highly disordered THF of solvation was also confined in the asymmetric unit, resulting in a poor quality structure. Details are included as Supporting Information, but not reported here, except for selected metrical parameters for the inner coordination sphere of Ni for comparison with **3** and **5**.

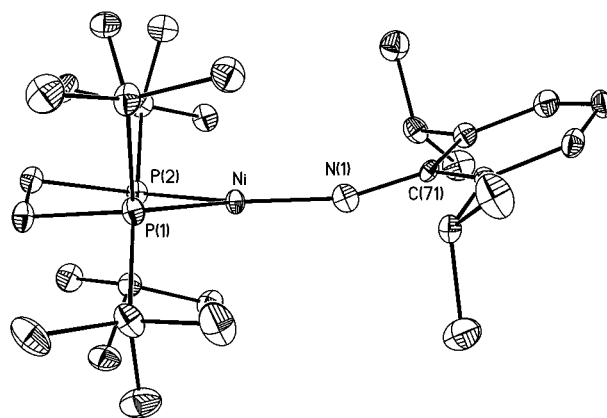


**Figure 2.** A perspective view of the molecular structure of **5** showing the atom-labeling scheme. H-atoms have been omitted for clarity. Selected metrical parameters: Ni–P(1) = 2.1815(8), Ni–P(2) = 2.1887(8), Ni–N(1) = 1.702(2), N(1)–C(71) = 1.355(3) Å; P(1)–Ni–P(2) = 90.94(3), P(1)–Ni–N(1) = 132.50(7), P(2)–Ni–N(1) = 136.46(7), Ni–N(1)–C(71) = 162.8(2)°.

Treatment of THF solutions of **4** with sodium bis(trimethylsilyl)amide at  $-35$  °C results in deprotonation of **4** at nitrogen, affording emerald-green crystals of the diamagnetic arylimido complex (dtbpe)Ni{N(2,6-(CHMe<sub>2</sub>)<sub>2</sub>C<sub>6</sub>H<sub>3</sub>)} (**5**) in 65% isolated yield. **5** was characterized by elemental analysis and IR and NMR (<sup>1</sup>H, <sup>13</sup>C, <sup>31</sup>P) spectroscopy,<sup>13</sup> and its monomeric structure was confirmed by single-crystal X-ray diffraction.<sup>19</sup>

The molecular structure of **5** is shown in Figure 2. The most salient structural features are a planar, three-coordinate nickel(II) center and a terminal imido ligand with a short Ni–N(1) bond (1.702(2) Å). The Ni–N(1) bond length is comparable to the value of 1.68 Å predicted by Pauling for a Ni–N bond order of two<sup>20</sup> and is consistent with a symmetry-allowed  $\pi$ -bonding interaction between a nitrogen lone pair and the empty in-plane Ni d-orbital of  $\pi$ -symmetry. The imido ligand is significantly bent at nitrogen (Ni–N(1)–C(71) = 162.8(2)°) out of the Ni coordination plane (as required by the in-plane  $\pi$ -bond). Steric interactions between the imido's aryl substituent and the phosphine's *tert*-Bu groups might be responsible for preventing this angle from being more acute.

In summary, we have shown that a cationic Ni(II)–amido complex can serve as a precursor to a Ni(II)–imido complex containing a terminal imido moiety. It is noteworthy that while **5** is air-sensitive, it does not exhibit unusual thermal instability (in fact, it is thermally robust), and it is somewhat surprising that related three-coordinate complexes of Ni(II) with hard  $\pi$ -donor ligands have not been previously prepared. We are currently exploring the reaction chemistries of these three-coordinate nickel complexes.

**Acknowledgment.** We are grateful to the National Science Foundation (CHE-9816341) for financial support of this research, to Dr. Ian Steele for assistance with crystallography, to Daniel Haines for assistance with electrochemical measurements, and to Cheslan Simpson and Ryan DaRe for insightful discussions.

**Supporting Information Available:** Experimental, spectroscopic, and analytical details; crystallographic details; atomic coordinates; bond angles and distances; anisotropic thermal parameters; hydrogen atom coordinates; least-squares planes; torsion angles (PDF). This material is available free of charge via the Internet at <http://pubs.acs.org>.

JA010358A

(19) Crystal data for **5**: C<sub>30</sub>H<sub>57</sub>NNiP<sub>2</sub>, triclinic,  $P\bar{1}$ ,  $a = 10.8639(10)$  Å,  $b = 11.1092(10)$  Å,  $c = 14.5704(14)$  Å,  $\alpha = 67.700(2)^\circ$ ,  $\beta = 72.419(2)^\circ$ ,  $\gamma = 75.351(2)^\circ$ ,  $Z = 2$ ,  $\mu(\text{Mo K}\alpha) = 7.56 \text{ cm}^{-1}$ ,  $T = 100 \text{ K}$ ,  $V = 1531.8(2) \text{ \AA}^3$ ,  $\lambda = 0.71073 \text{ \AA}$ ,  $D_c = 1.198 \text{ mg/mm}^3$ . Of 8973 data collected (emerald green crystal,  $1.55 \leq \theta \leq 28.28$ ) 6199 were independent and observed with  $I > 2\sigma(I)$ . All non-hydrogen atoms were anisotropically refined, and hydrogen atoms were placed in idealized positions.  $R(F) = 0.0475$  and  $R(wF^2) = 0.0947$ .

(20) The Pauling and Schomaker–Stevenson covalent radii, with corrections for electronegativity, predict bond lengths of 1.80 and 1.68 Å for Ni–N single and double bonds, respectively. Pauling, L. *The Nature of the Chemical Bond*, 3rd ed.; Cornell University Press: Ithaca, NY, 1960.